Progress In Electromagnetics Research C, Vol. 171, 374–383, 2026

PIER C

(Received 21 April 2026, Accepted 11 June 2026, Scheduled 29 June 2026)

Sensitivity Analysis of SAR Performance in a 2 GHz Narrow-Band Microstrip Antenna Designed for Breast Cancer Detection

Rachida Boulerbah[1,*], Abdelhalim Chaabane[2], Djelloul Aissaoui[1], and Abderrezak Khalfallaoui[3]

[1]*Laboratory of Telecommunications and Smart Systems, Ziane Achour University of Djelfa, Djelfa 17000, Algeria*
[2]*Faculty of Technology, Department of Electronics, University of Ferhat Abbas Setif-1, Setif 19000, Algeria*
[3]*Laboratory of Telecommunications-LT, University of 8 May 1945 Guelma, Guelma 24000, Algeria*

ABSTRACT: Malignant breast tumors differ greatly from healthy tissues in terms of their electrical properties. The specific absorption rate (SAR), which utilizes dielectric properties, including conductivity and permittivity, is a crucial metric for identifying malignant tissue. The use of narrow-band radar technology has shown promise in this regard. In this study, a mono-static, narrow-band, high-directivity printed patch antenna was designed and fabricated on a Rogers RO4350B substrate ($\varepsilon_r = 3.48$, loss tangent = 0.0037) with dimensions of $70 \times 55 \times 1.52\,\text{mm}^3$ and a $50\,\Omega$ feed line, operating at 2 GHz to ensure an optimal balance between penetration depth and spatial resolution. A three-dimensional breast phantom (radius 50 mm) was modeled in CST Microwave Studio to evaluate the SAR distribution under microwave exposure. The results consistently showed elevated SAR values in malignant regions, with a direct correlation with tumor size, enabling accurate tumor localization based on the coordinates of the maximum SAR. Crucially, the maximum SAR values (4.3708 W/kg for 1-g and 2.4388 W/kg for 10-g tissue) remain within the IEEE controlled-environment safety limits. Powered by the proposed antenna, this SAR-based approach offers a safe, non-ionizing, and potentially effective technique for detecting small or deeply located breast tumors, confirming that diagnostic capability is achieved without any compromise to patient safety.

1. INTRODUCTION

The high incidence of breast cancer is projected to reach 316,950 new cases in the United States alone. Women in 2025 highlight the critical need for advanced diagnostic technologies [1]. Approximately 42,170 deaths from female breast cancer are projected for the same year. On a global scale, cancer remains one of the leading causes of mortality, accounting for millions of deaths annually according to the World Health Organization (WHO) [2]. Among the various diagnostic platforms, medical imaging modalities are key components in cancer diagnosis and treatment, as they provide otherwise unobtainable internal information and high-resolution imaging of anatomical structures.

Breast imaging systems generally comprise the most widely used diagnostic techniques for breast tumor detection, including mammography [3], magnetic resonance imaging (MRI) [4], ultrasound (US) [5], optical imaging (OI), and photo-acoustic imaging (PAI), with the latter three modalities further explaining recent devices in [6]. The shortcomings of these conventional techniques have led to intensive research on the development of new microwave-based techniques [7] and portable non-invasive technologies [8]. Recently, smart graphene-enhanced ceramic material refractive index sensors optimized with machine learning have been proposed for highly sensitive breast cancer detection [9]. Owing to their noninvasive nature and the absence of ionizing radiation, microwave imaging (MWI) techniques may be a promising option for breast cancer detection [10].

Narrow-band radar techniques are gaining prominence in breast cancer detection, offering advantages in terms of system simplicity, directional operation, and tissue penetration over ultra-wideband systems [11]. This study employed a 2 GHz narrow-band design to optimize the microwave-tissue interaction. Although the 2.45 GHz Industrial, Scientific, and Medical (ISM) band provides regulatory advantages [12], its higher attenuation and susceptibility to interference from common wireless devices reduce the penetration depth and detection sensitivity. The implemented microstrip patch antenna features a dielectric substrate with a radiating patch and a ground plane [13], avoiding thin substrates with high transmittance to maintain efficiency. Specific Absorption Rate (SAR) is a crucial diagnostic metric, enabling tumor localization by detecting elevated energy absorption in malignant tissue. The selected 2 GHz operating frequency represents an optimal compromise between the spatial resolution and penetration depth for effective SAR-based breast tumor imaging.

Although ultra-wideband (UWB) systems are widely employed in microwave breast imaging to achieve high spatial resolution [11], narrow-band operation offers specific advantages that justify its selection in this study [12]. The comparative trade-offs are as follows: First, at 2 GHz, electromagnetic waves penetrate deeper into biological tissues than the

* Corresponding author: Rachida Boulerbah (rachida.boulerbah@univ-djelfa.dz).

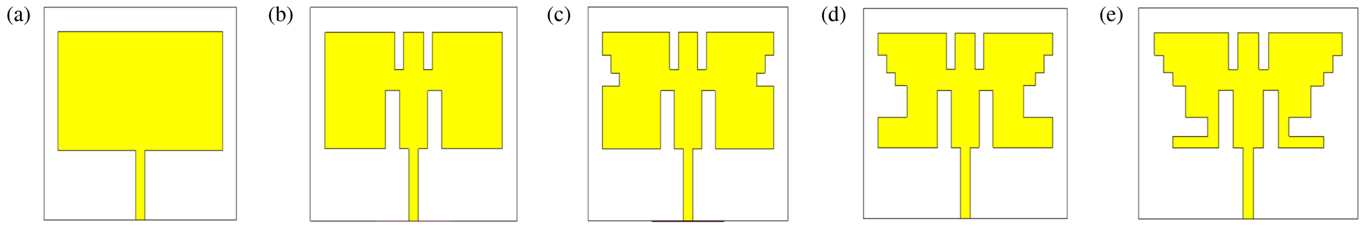

FIGURE 1. Evolution of the proposed antenna through successive design stages (a), (b), (c), (d), (e) to the final suggested design.

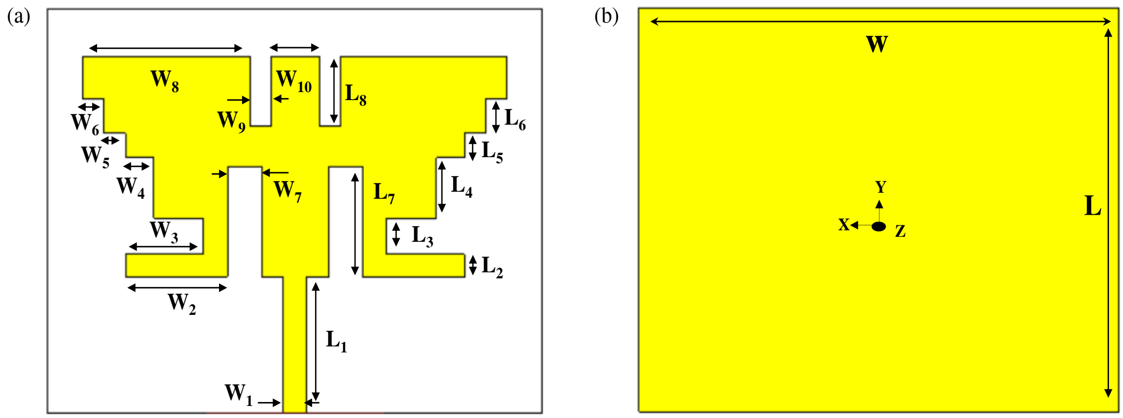

FIGURE 2. Configuration of the designed patch antenna at 2 GHz: (a) View from the front and (b) view from the back.

higher frequencies (e.g., 3.1–10.6 GHz) used in UWB systems, a critical feature for detecting deeply seated tumors. Second, narrow-band systems require simpler electronics, lower sampling rates, and less complex signal processing, facilitating the development of portable and low-cost diagnostic devices. Third, narrow-band signals are less susceptible to frequency-dependent dispersion in lossy breast tissue, a phenomenon that degrades range resolution in UWB systems. Fourth, our detection method relies on dielectric contrast rather than the time of flight resolution. Fifth, the 2 GHz band experiences reduced external interference compared to more congested frequencies. The primary trade-off is lower spatial resolution relative to UWB, which is acceptable given the diagnostic objective of tumor presence detection and coarse localization.

While SAR-based breast tumor detection has been explored in prior literature, the present work introduces several distinct contributions that advance the state of the art. First, unlike most existing narrow-band systems operating at 2.45 GHz or in the UWB range, we employ a 2 GHz operating frequency, providing deeper tissue penetration and reduced external interference. Second, the proposed patch antenna achieves a compact footprint of $70 \times 55 \times 1.52\,\text{mm}^3$ with a simulated gain of 3.71 dBi, and experimental validation of S_{11} shows good agreement with simulations. Third, we demonstrate a direct SAR to tumor localization method requiring no complex beamforming, achieving lateral accuracy within 23 mm. Fourth, we quantify SAR sensitivity for tumors as small as 5 mm in radius. Fifth, we quantify a systematic axial displacement of 6.89 mm, attributed to wave refraction, demonstrating spatial correlation of SAR with tumor position. Collectively, these contributions establish the proposed 2 GHz antenna as a practical solution for breast tumor detection.

The remainder of this paper is organized as follows. In Section 2, we describe the antenna design and fabrication process, followed by an explanation of the design of the breast-simulating phantom, including the permittivity and conductivity of its tumor and layers. In Section 3, we compute and analyze the SAR for tumors of different sizes and positions, as well as the spatial precision in tumor detection and localization. The performance of the proposed antenna is compared with that of existing antennas. Finally, we conclude the paper by summarizing the key findings in Section 4.

2. METHODOLOGY

2.1. Antenna Performance Analysis

The suggested antenna was designed using a Rogers 4350B substrate, which has a dielectric constant of 3.48 and $\tan\delta = 0.0037$. Both sides of the substrate were laminated with 0.035 mm copper layers. A $50\,\Omega$ impedance feed line was integrated into the design as the feeding port. The substrate thickness is 1.52 mm, and the antenna dimensions were optimized to $70 \times 55\,\text{mm}^2$ using CST Microwave Studio for simulation and design. Based on this design, Fig. 1 shows the progression of the proposed antenna through the design stages, while Fig. 2 illustrates the geometric configuration of the narrow-band patch antenna optimized for operation at 2 GHz, with its dimensional parameters detailed in Table 1. The corresponding reflection coefficients for the different designs are shown in Fig. 3.

TABLE 1. Optimized dimensions of the suggested antenna in mm.

Parameter	W	L	W_1	L_1	W_2	L_2	W_3	L_3	W_4	L_4
Value (mm)	70	55	3.3	18.6	14.5	3	11	5	4	8.2
Parameter	W_5	L_5	W_6	L_6	W_7	L_7	W_8	L_8	W_9	W_{10}
Value (mm)	3	3.36	3	4.6	4.8	15	23.6	9.6	6.8	3

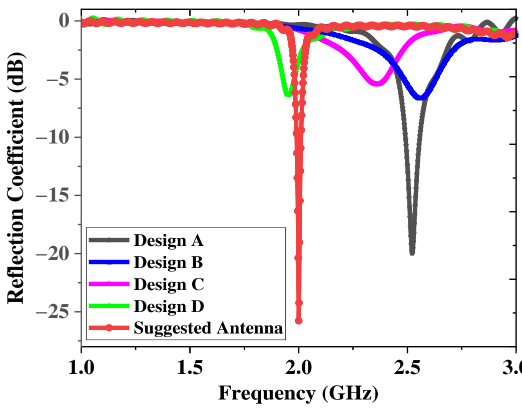

FIGURE 3. Comparison of the reflection coefficient of the suggested antenna with the initial reference antennas.

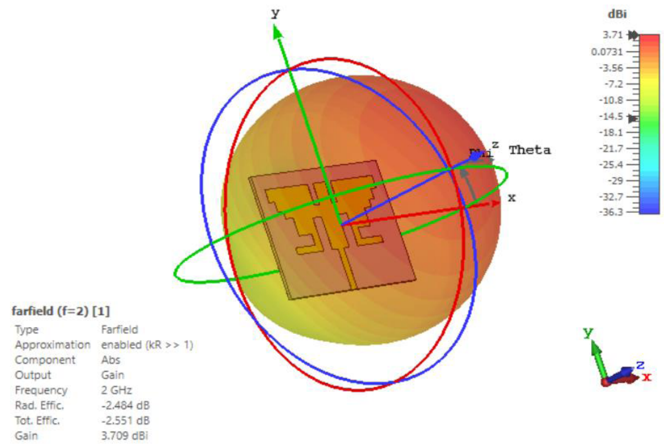

FIGURE 5. Gain of the suggested antenna.

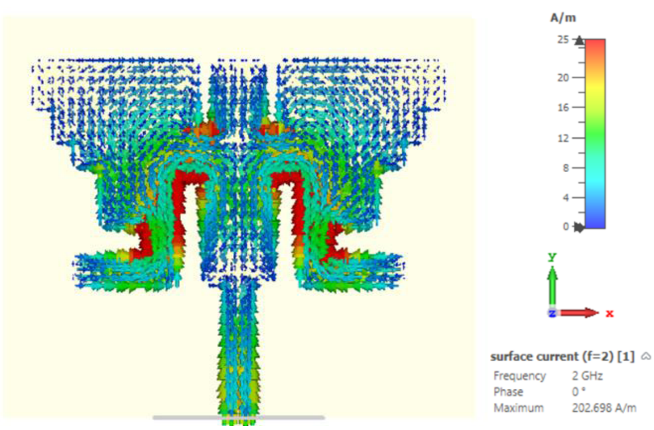

FIGURE 4. Current distribution on the suggested antenna at 2 GHz.

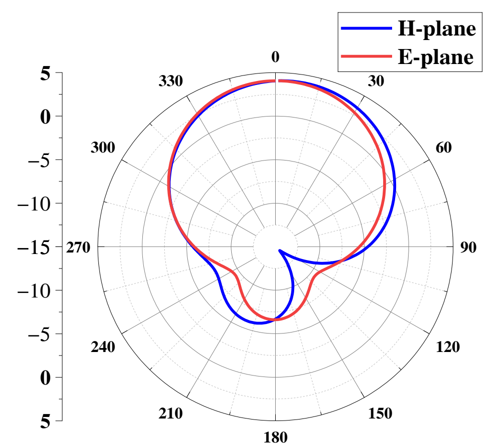

FIGURE 6. Simulated radiation patterns of the suggested antenna (H-E plane) at 2 GHz.

To further evaluate the antenna's behavior, Fig. 4 illustrates the surface current distribution of the proposed directive antenna at 2 GHz, revealing that the strongest currents are concentrated along the feed and patch edges — an indication of efficient excitation of the radiating element. The corresponding realized gain, shown in Fig. 5, is approximately 3.709 dBi. Moreover, Fig. 6 shows the simulated H–plane and E-plane radiation patterns, demonstrating a highly stable directional mainlobe and low side-lobe levels, which corroborate the antenna's suitability for focused MWI interaction with the breast tissue.

2.2. Antenna Fabrication and Experimental Validation

Following the design phase, the antenna was fabricated to validate its performance through empirical measurements. The prototype, photographed in Fig. 7, was realized using an LPKF Proto Mat E44 system on a 1.52 mm-thick Rogers 4350B substrate, with final board dimensions of $70 \times 55\,mm^2$. The experimental setup for assessing the reflection coefficient in a free-space environment, based on an R&S®ZNB Vector Network Analyzer, is illustrated in Fig. 8. The measured results were then compared with the simulated data, as shown in Fig. 9. The close alignment between the two curves indicates the high fidelity of the simulation model to the physical reality. Quantitatively, the measured impedance bandwidth was 30 MHz (1.96 to 1.99 GHz), which showed a good correlation with the simulated 22 MHz bandwidth (1.99 to 2.012 GHz). The slight frequency shift and bandwidth variation are within acceptable margins and are commonly caused by minor imperfections in the fabrication process and the influence of the SMA connector.

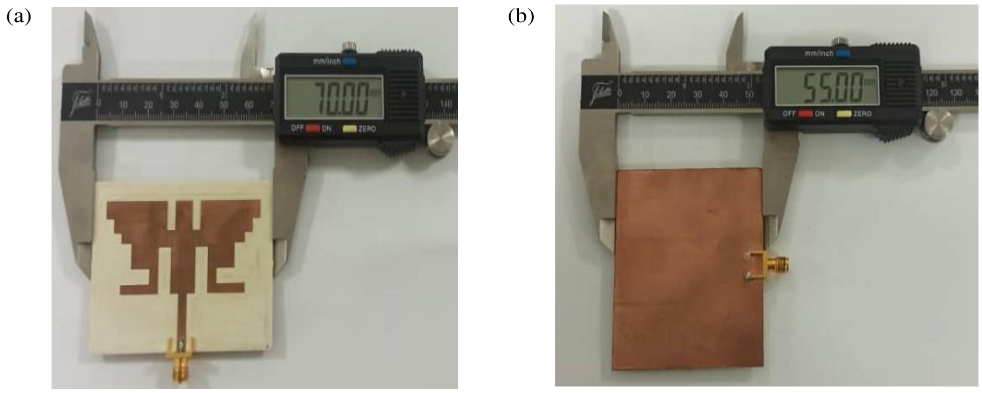

FIGURE 7. Fabricated model of the suggested narrow-band patch antenna: (a) front and (b) back perspectives.

FIGURE 8. Reflection coefficient setup measurement of the antenna 2 GHz in free space.

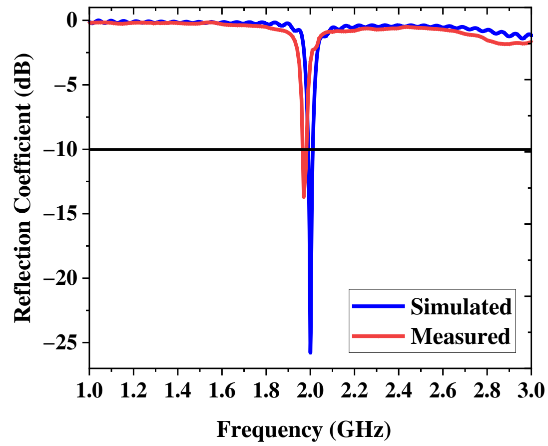

FIGURE 9. Simulated and experimentally obtained reflection coefficients of the suggested antenna in free space.

2.3. Breast Phantom Model

Several breast models have been developed to simulate the heterogeneous nature of human tissues [14]. As different tissues possess different electrical properties and absorb microwave energy at varying levels, differences in operating frequency significantly influence the dielectric behavior of biological media. Quantitative MWI estimates the dielectric parameters using the contrast in complex permittivity. To address the complex composition and structure of biological tissues, a widely adopted four-Cole-Cole model was developed. This parametric model describes four different mechanisms of dispersion within biological tissues, characterizes frequency-dependent permittivity and conductivity across a broad spectrum [15], from hertz to gigahertz, and is expressed as Eq. (1):

$$\varepsilon(\omega)=\varepsilon'(\omega)+j\varepsilon''(\omega)=\sum_{n=1}^{4}\varepsilon_\infty+\frac{\Delta\varepsilon_n}{1+(j\omega\tau_n)^{1-\alpha_n}} + \frac{\sigma_i}{j\omega\varepsilon_0}. \quad (1)$$

The loss factor represents a material's ability to absorb microwave energy, whereas the real part corresponds to its capacity to store microwave energy. The dispersion magnitude is expressed as:

$$\Delta\varepsilon_n=\varepsilon_s-\varepsilon_\infty,$$

where ε_∞ is the permittivity at high frequency, ε_s the static permittivity, ω the angular frequency (rad/s), τ the relaxation time constant (s), σ_i the static ionic conductivity (S/m), α the distribution parameter, and ε_0 the permittivity of free space.

The fundamental principle of MWI breast cancer detection is based on the high contrast between the dielectric properties of normal and malignant tissues [16]. This technique involves the use of a monostatic radar imaging system with a single antenna acting as both the receiver and transmitter to detect tumors. The antenna emits microwave pulses that penetrate the breast, allowing multiple points within the breast phantom to be scanned by the antenna. The interactions thus generated are analyzed in the form of SAR distributions [17], which highlight areas of high energy absorption that correlate with potential tumor sites, enabling more precise and noninvasive tumor localization.

A multilayer hemispherical breast model composed of skin, fatty tissue, and glandular tissue was simulated, as illustrated in Fig. 10, in contrast to another study [18] that used voxel data in CST. The proposed multilayer model, while not capturing all anatomical complexities such as irregular glandular dis-

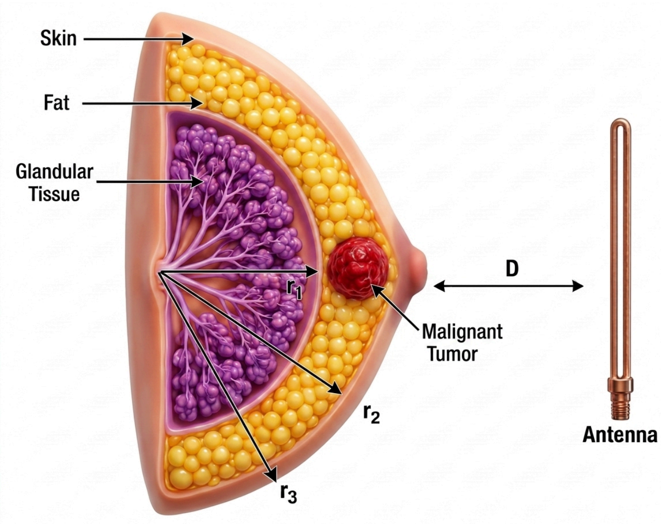

FIGURE 10. 3-D hemispherical breast model with radii $r_1 = 50$ mm, $r_2 = 46$ mm, and $r_3 = 30$ mm, including variable tumor size.

tributions or Cooper's ligaments, represents a well-established compromise between anatomical realism and computational efficiency. The dielectric properties of each layer (skin, fat, fibroglandular) are frequency-dependent and derived from the four-Cole-Cole model [15], ensuring electromagnetic accuracy. The antenna is positioned $D = 20$ mm away from the breast. The model has a total height of 50 mm, with layer radii defined as $r_1 = 50$ mm, $r_2 = 46$ mm, and $r_3 = 30$ mm. Malignant tumors are represented as spherical layers with different radii, providing a more anatomically realistic representation than homogeneous models. The dielectric properties of each layer are detailed in Table 2 [19]. This configuration reduces edge reflections and maintains a uniform antenna-to-tissue distance by approximating the natural breast curvature. Consequently, the resulting scattering parameters and SAR distributions offer a realistic evaluation of the antenna's tumor detection performance. However, a key simplification in the present study is that the dielectric properties of the malignant tumor were taken as fixed values from the literature, corresponding to a generic cancerous state. This is an important caveat because, in reality, the permittivity and conductivity of breast tumors vary with the degree of pathology, depending on factors such as cellular density, necrosis, fibrosis, and tumor grade. Beyond this dielectric simplification, the magnetic permeability of all tissues is assumed to be that of free space, with relative permeability equal to 1, which is standard for non-magnetic biological tissues at microwave frequencies.

TABLE 2. Breast phantom tissue characteristics at 2 GHz [19].

Tissue	σ (S/m)	ε	ρ (kg/m^3)	R (mm)
Skin	3.6	38	1010	50
Fat	0.2	11	928	46
Fibro-gland	0.8	18	1030	30
Tumor	4.0	56	1100	Variable

3. RESULTS AND DISCUSSION

3.1. Specific Absorption Rate (SAR) Evaluation

To assess its application in breast cancer detection, the proposed antenna was integrated into a numerical imaging system. The key metric for evaluating patient safety in such systems is the SAR. According to the IEEE standard, SAR quantifies the rate at which energy is absorbed per unit mass of biological tissue [20]. Formally, it is defined as the time derivative of the incremental energy (dW) absorbed by an incremental mass (dm) contained in a volume element (dV) of density (ρ) as follows:

$$\text{SAR} = \frac{d}{dt}\left(\frac{dW}{dm}\right) = \frac{d}{dt}\left(\frac{dW}{\rho dV}\right) \tag{2}$$

SAR is used to diagnose abnormalities in human breast tissue by quantifying the electromagnetic energy absorbed by the biological tissues. Locations with high SAR values indicate the potential presence of a tumor and assist in identifying the location where it occurs. Tissue heating is caused by absorbed energy, and SAR is used to directly measure the heating. Thus, the assessment is aimed at regions of maximum absorption due to the presence of tumors. This method highlights the effectiveness of using peak SAR coordinates to find tumor positions within the breast. The absorbed power was compared between normal breast tissue and breast tissue with tumors using the maximum SAR values obtained for various tumor positions, and frequency ranges [21]. The SAR expression is provided in Eq. (3).

$$\text{SAR (W/Kg)} = \frac{\sigma |E|^2}{\rho} \tag{3}$$

Here, SAR denotes the Specific Absorption Rate (W/kg), σ the tissue conductivity (S/m), E the internal electric field (V/m), and ρ the mass density (kg/m^3). In this study, however, SAR is employed as an electromagnetic diagnostic metric for tumor localization based on dielectric contrast, rather than as a predictor of thermal elevation. Temperature rise simulation is beyond the scope of this detection-focused investigation.

Table 3 summarizes the regulatory limits for local SAR, including whole-body SAR (SAR_{WB}), 1 g, and 10 g of tissue for both controlled and uncontrolled exposure environments. These regulatory limits are essential points of reference to ensure that the diagnostic and therapeutic applications of electromagnetic fields, such as breast cancer detection equipment, operate according to the required safety standards.

3.2. Analysis of Tumor Location Detection and SAR Performance

The homogeneous breast phantom was illuminated with a narrow-band excitation from the suggested antenna, and the maximum SAR, together with the 1-g and 10-g averaged SAR values and their spatial coordinates, was evaluated at 2 GHz. The results, summarized in Table 4, compare the SAR distribution between normal and tumor-bearing breast models. In the simulations, the tumor was positioned at $(0, 0, 30)$ mm; the distance between the antenna and breast phantom is

TABLE 3. SAR exposure limits in different conditions (WB = whole body, 1-g and 10-g tissue) [21].

	Controlled Environment (W/kg)	Uncontrolled Environment (W/kg)
SAR_{WB}	0.4	0.08
$SAR_{1\text{-g}}$	8.0	1.6
$SAR_{10\text{-g}}$	20.0	4.0

TABLE 4. Comparison of SAR distribution between healthy and tumor-bearing breast models as a function of tumor size at 2 GHz, with the tumor positioned at $(0, 0, 30)$ mm.

Tumor Radius	10-g Analysis		1-g Analysis	
	Max SAR (W/kg)	Max Location (x, y, z) [mm]	Max SAR (W/kg)	Max Location (x, y, z) [mm]
Without Tumor	0.6857	$(3.10, -2.24, 23.56)$	1.5184	$(3.10, -6.71, 23.56)$
5 mm	1.5738	$(0.27, 0.31, 32.79)$	3.3508	$(0.27, 0.31, 26.70)$
6 mm	1.6095	$(0.27, 0.30, 21.89)$	3.3923	$(0.27, 0.30, 26.70)$
7 mm	1.6690	$(0.27, 0.30, 32.79)$	3.5555	$(0.27, 0.30, 26.70)$
8 mm	1.7126	$(0.27, 0.30, 32.79)$	3.6615	$(0.27, 0.30, 26.70)$
12 mm	1.8328	$(0.27, -0.26, 21.89)$	3.7171	$(0.27, 0.30, 21.89)$
14 mm	1.9411	$(0.27, 0.30, 21.89)$	3.7681	$(0.27, 0.30, 26.67)$
15 mm	2.0196	$(0.27, 0.30, 21.89)$	3.8838	$(0.27, 0.30, 26.65)$
16 mm	2.1569	$(-0.27, 0.30, 21.89)$	4.1222	$(0.27, 0.30, 21.89)$
17 mm	2.2275	$(0.27, 0.30, 32.68)$	4.2167	$(0.27, 0.30, 26.68)$
18 mm	2.3079	$(-0.27, 0.30, 21.89)$	4.2961	$(0.27, 0.30, 26.65)$
19 mm	2.3901	$(-0.27, 0.30, 21.89)$	4.3713	$(-0.27, -0.26, 21.89)$
20 mm	2.4388	$(0.27, 0.30, 32.49)$	4.3708	$(0.27, 0.30, 26.68)$

$D = 20$ mm; and the computed SAR peak locations were analyzed. The findings clearly indicate that the presence of a tumor results in significantly higher SAR values compared to the tumor-free case. For the healthy breast model, the highest SAR values were 0.6857 W/kg (10 g) and 1.5184 W/kg (1 g). In contrast, for tumor-bearing models with radii ranging from 5 to 20 mm, the maximum 10-g SAR values increased from 1.5738 to 2.4388 W/kg, while the corresponding 1-g SAR values ranged from 3.3508 to 4.3708 W/kg. In [22], a voxel-based breast phantom was used to investigate SAR distribution at 2.45 GHz using an aperture-coupled patch antenna under standards of 1-g and 10-g average. The study demonstrated a monotonic increase in SAR with tumor growth, increasing from 2.2636 W/kg (1 g) and 0.9599 W/kg (10 g) in the absence of a tumor to 6.2252 W/kg and 3.4429 W/kg, respectively, for a tumor radius of 20 mm.

Furthermore, when the tumor was located at (0, 0, 30) mm in the present study, the SAR distribution exhibited a strong spatial correlation with the implanted tumor. In Table 4, the maximum SAR in the tumor-free breast appeared at the displaced coordinates, whereas in the tumor-bearing models, the SAR hotspot consistently coincided with the tumor position. Specifically, for 10-g averaging, the maxima were concentrated near (0.27, 0.30, 21, or 32) mm, while for 1-g averaging, they were observed around (0.27, 0.31, 21, or 26) mm. This spatial correspondence between the tumor location and SAR maxima validates the potential of SAR-based analysis as a reliable tool for tumor localization.

Figures 11 to 14 illustrate the SAR distributions for cases without and with tumors of different radii. Specifically, Fig. 11 presents the healthy breast case (no tumor); Fig. 12 corresponds to a tumor radius of $R = 5$ mm, Fig. 13 to $R = 15$ mm, and Fig. 14 to $R = 20$ mm. In each figure, the two subgraphs show the 10-g and 1-g averaged SAR distributions, respectively, where the highest SAR is represented by the red region localized at the tumor center. A comparative plot of these results is provided in Fig. 15, further confirming enhanced energy absorption in the tumor-bearing tissue. This confirmation is based on simulated SAR distributions, whereas the experimental validation is focused on the reflection coefficient. Consequently, the SAR distributions and tumor localization performance are evaluated through simulations, as the dedicated field-mapping setups required for experimental verification are not part of the present investigation.

Comparing the simulated SAR values in Table 4 with the IEEE exposure limits summarized in Table 3, the maximum 10-g SAR value (2.4388 W/kg for a 20 mm tumor) remains below both the uncontrolled (4.0 W/kg) and controlled (20.0 W/kg) environment limits. The maximum 1-g SAR value (4.3708 W/kg) is below the controlled environment limit (8.0 W/kg) but exceeds the uncontrolled limit (1.6 W/kg). This is acceptable for clinical diagnostic applications, where the device operates in controlled settings (trained personnel, limited patient exposure duration, typically a few minutes). Thus, the proposed microwave-based detection method satisfies recognized safety standards for controlled environments.

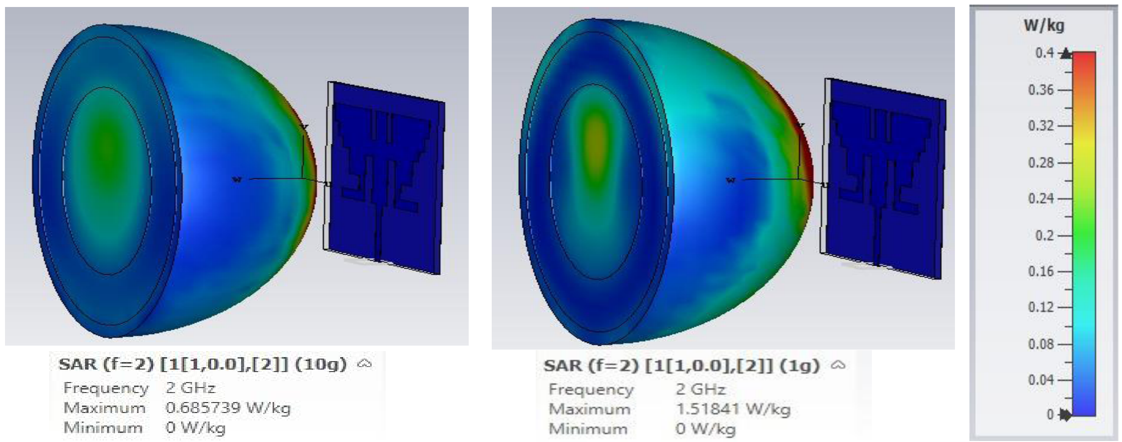

FIGURE 11. SAR healthy breast phantom.

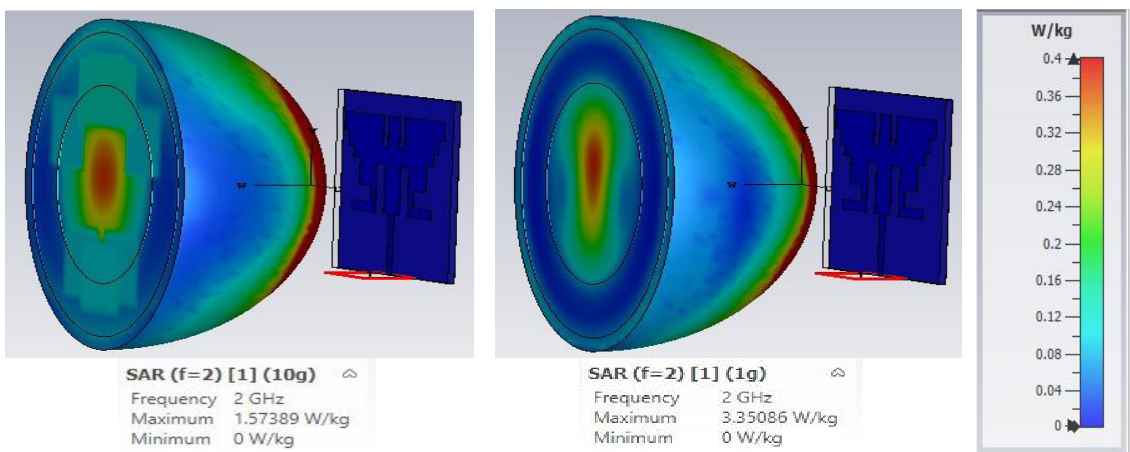

FIGURE 12. SAR breast with tumor radius $R = 5$ mm.

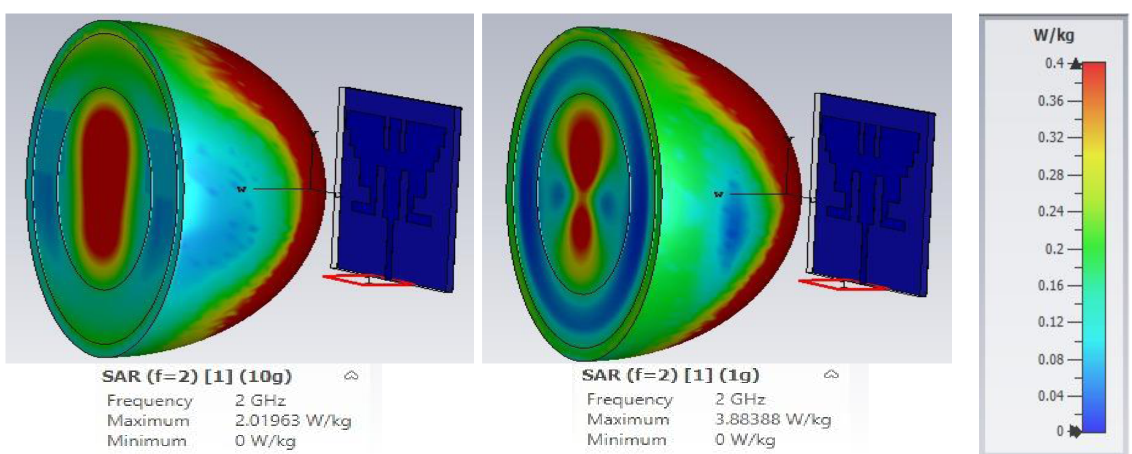

FIGURE 13. SAR breast with tumor radius $R = 15$ mm.

3.3. Spatial Precision in Tumor Detection and Localization

The spatial targeting performance of the system was evaluated under controlled conditions with a fixed tumor radius of $R = 10$ mm and a constant separation of 20 mm between the antenna and breast phantom surface. As evidenced by comprehensive testing across multiple tumor coordinates, the configuration demonstrates reliable detection capability despite the inherent challenges of focal depth control. The consistent antenna-to-phantom distance ensured stable wave propagation characteristics, whereas the standardized tumor size provided a uniform reference for assessing localization accuracy across varying spatial positions.

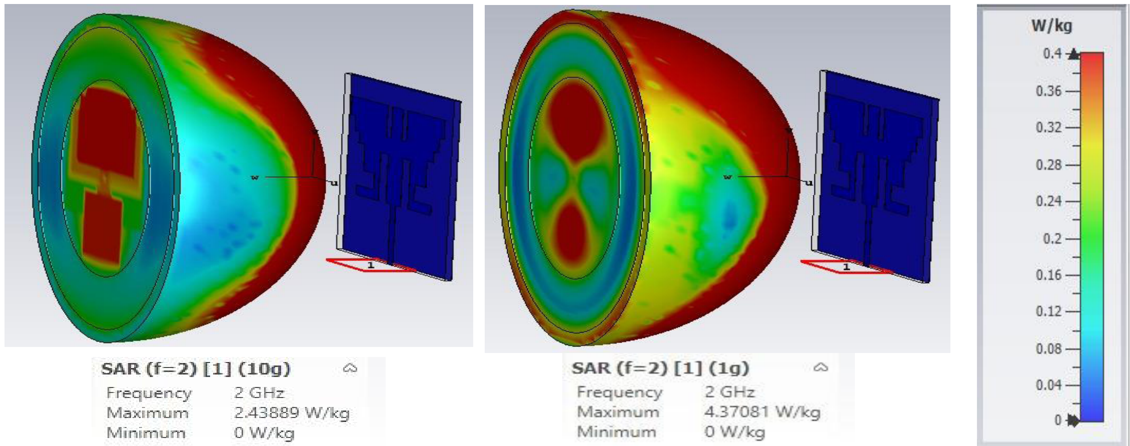

FIGURE 14. SAR breast with tumor radius $R = 20\,\text{mm}$.

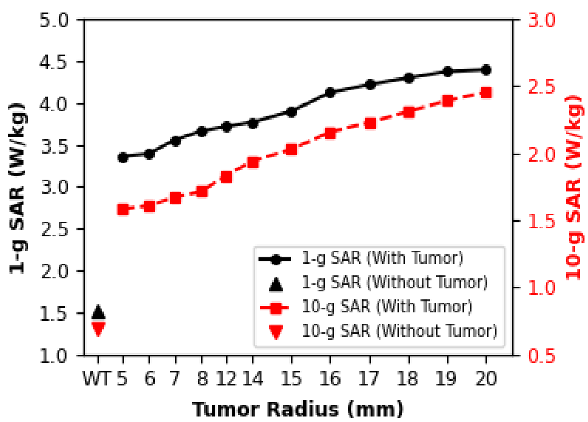

FIGURE 15. SAR values corresponding to different tumor radii (1 and 10-g analysis) for a tumor located at the coordinate (0, 0, 30).

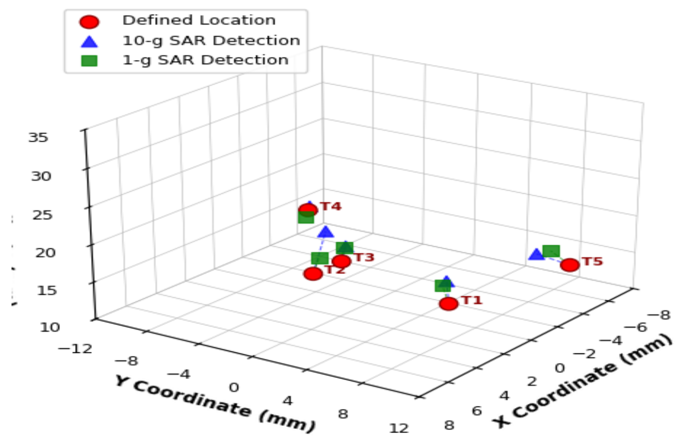

FIGURE 16. Comparison between defined and simulated locations for $R = 10\,\text{mm}$ tumor radius.

TABLE 5. SAR-based tumor localization: displacement between defined and simulated focal points.

Defined tumor coordinates (mm)	10-g Analysis		1-g Analysis	
	Max SAR (W/kg)	Max at (x, y, z) [mm]	Max SAR (W/kg)	Max at (x, y, z) [mm]
(2, 8, 15)	2.324	(−0.27, 5.14, 21.89)	4.022	(1.37, 5.75, 21.89)
(2, −2, 15)	2.453	(−0.27, −1.21, 32.49)	4.336	(1.37, −1.21, 21.89)
(0, −2, 15)	2.435	(−0.27, −1.21, 21.89)	4.309	(0.27, −1.21, 21.89)
(−5, −10, 15)	2.087	(−0.82, −4.99, 21.89)	3.521	(3.62, −1.26, 21.89)
(−5, 10, 15)	2.174	(−0.82, 5.73, 21.89)	3.667	(−3.11, 6.95, 21.89)

The analysis of resulting energy deposition patterns in Table 5 reveals a consistent spatial relationship between intended tumor locations and detected positions. The system successfully identifies tumor presence across all tested coordinates, with lateral detection accuracy within 2–3 mm of target positions in both x and y dimensions. However, a systematic axial displacement is observed, with the focal point consistently appearing at approximately 21.89 mm depth rather than the intended 15 mm target depth. This reproducible 6.89 mm depth offset occurs despite the fixed antenna placement and tumor dimensions, suggesting a predictable refraction or focusing artifact within the phantom medium. The combination of fixed tumor size and standardized antenna distance provides valuable insights into the system's beam-forming characteristics. The consistent lateral accuracy coupled with predictable depth displacement indicates that the observed targeting error is systematic rather than random, making it amenable to correction through computational refinement of the focusing algorithm. These findings confirm the system's fundamental detection capability while highlighting the importance of accounting for depth-specific propagation effects in treatment planning, particularly given the fixed geometrical constraints of the

TABLE 6. Performance and feature comparison with state-of-the-art breast cancer detection antennas.

Aspect	Aldhaeebi et al. [23]	Mahfuz et al. [24]	Elsaadi et al. [25]	Bhavani et al. [26]	Proposed Work
Antenna Type	1×4 Loop	Tuning Fork	Rectangular Patch	QMSIW	Microstrip Patch
Frequency (GHz)	1.108	5.8	2.45	2.6	2.0
Substrate	RO4003C	Jeans	FR-4	RT Duroid 5880	RO4350B
Antenna Size (mm^2)	125×51	40×45	50×50	33×26	70×55
Gain (dBi)	N/A	N/A	N/A	3.46	3.71
Breast Model	Numerical	Multilayer	Multilayer	Multilayer / Fabricated	Multilayer
Detection Metric	S_{11}	S_{11}, SAR	SAR	S_{11}, SAR	SAR
Max. SAR (W/kg)	N/A	< 2	< 2	< 2	< 2
Tumor Radius (mm)	7, 15, 20	10, 20, 30	10, 50	6, 7, 8, 10	5

experimental setup. Subsequent investigations will incorporate patient-derived tumor morphologies (irregular, spiculated, and lobulated shapes) and heterogeneous breast phantoms with glandular structures to validate the generalizability of the SAR-based detection method.

A comparative analysis between the actual tumor coordinates and simulated maximum absorbed power locations, as visualized in the two-dimensional representation of Fig. 16, revealed a robust but imperfect localization capability. The system consistently detected the general vicinity of the tumor, with the focal point of energy deposition reliably appearing in close lateral proximity to the intended target, typically within a few millimeters of the target. However, a systematic and reproducible axial displacement was observed, where the depth of the simulated hotspot consistently deviated from the prescribed tumor depth. This predictable spatial offset, evident across multiple tumor positions, indicates a correctable error in the beamforming algorithm, which is likely attributable to wave propagation effects within the heterogeneous phantom medium. The results conclusively demonstrate the system's fundamental capacity for accurate tumor detection while precisely characterizing a deterministic targeting error that can be mitigated through subsequent algorithmic calibration, thereby enhancing precision for noninvasive therapeutic applications.

3.4. Comparative Evaluation

The designed antenna was compared with some recently developed breast cancer detection antennas to assess its performance in terms of SAR distribution, tumor detection accuracy, and operating frequency. The suggested antenna is more sensitive to small tumors than conventional designs, as it creates an improved SAR contrast between malignant and normal tissues. Its monostatic form and small size provide greater coverage with lower patient exposure. In addition, simulation results demonstrate that the newly designed antenna exhibits robust SAR localization for tumors of varying sizes and positions, outperforming existing designs in terms of detection reliability. Table 6 lists important parameters, such as frequency band, detection thresholds for different tumor sizes, maximum SAR, and overall detection efficiency, demonstrating the proposed antenna's excellence in real-world applications and safety.

4. CONCLUSION

This study has presented a directional 2 GHz narrow-band antenna on Rogers RO4350B for breast cancer detection. A multilayer hemispherical breast phantom was developed, and simulations confirmed tumor detection via absorbed power comparison. Maximum SAR coordinates reliably indicate tumor position (lateral accuracy 2–3 mm, axial displacement $\approx$ 6.89 mm due to refraction). 2-D SAR visualizations further confirm tumor-induced perturbation. Crucially, maximum SAR values (4.3708 W/kg for 1 g, 2.4388 W/kg for 10 g) remain within IEEE-controlled environment safety limits, ensuring patient safety. A heterogeneous breast model is recommended for future validation. These contributions, including narrow-band 2 GHz design, an SAR-based metric, quantified localization, and 2-D visualization, distinguish our approach from prior UWB-dominated literature. However, the present study is simulation-only; clinical claims are premature. Future work will incorporate frequency-dependent Cole-Cole models with stage specific parameters to assess SAR sensitivity to tumor dielectric variations, include varying tumor positions and patient-derived tumor morphologies (irregular, spiculated, lobulated), employ realistic phantoms with glandular and heterogeneous tissue properties, include robustness analysis with random permittivity/conductivity variations and different glandular distributions, develop a detailed methodology for extracting SAR maxima (e.g., peak detection, coordinate refinement), analyze potential false-positive scenarios (e.g., skin-layer focusing, glandular clusters, benign lesions), define normal-tissue absorption thresholds, conduct experimental SAR verification and clinical validation, and integrate machine learning-optimized sensors for improved accuracy.

ACKNOWLEDGEMENT

This work was supported by the Ministry of Higher Education and Scientific Research of Algeria as part of a research project (PRFU $N°$, A25N01UN240120220002).

REFERENCES

[1] American Cancer Society, "Cancer facts & figures 2025," Atlanta, GA, 2025. [Online]. Available: https://www.cancer.org/

content/dam/cancer-org/research/cancer-facts-and-statistics/annual-cancer-facts-and-figures/2025/2025-cancer-facts-and-figures-acs.pdf.

[2] World Health Organization, "Cancer fact sheet," Geneva, Switzerland, 2025. [Online]. Available: https://www.who.int/news-room/fact-sheets/detail/cancer.

[3] Hernström, V., V. Josefsson, H. Sartor, D. Schmidt, A.-M. Larsson, S. Hofvind, I. Andersson, A. Rosso, O. Hagberg, and K. Lång, "Screening performance and characteristics of breast cancer detected in the Mammography Screening with Artificial Intelligence trial (MASAI): A randomised, controlled, parallel-group, non-inferiority, single-blinded, screening accuracy study," *The Lancet Digital Health*, Vol. 7, No. 3, e175–e183, 2025.

[4] Eisen, A., G. G. Fletcher, S. Fienberg, R. George, C. Holloway, S. Kulkarni, J. M. Seely, and D. Muradali, "Breast magnetic resonance imaging for preoperative evaluation of breast cancer: A systematic review and meta-analysis," *Canadian Association of Radiologists Journal*, Vol. 75, No. 1, 118–135, 2024.

[5] Stout, N. K., D. L. Miglioretti, Y.-R. Su, C. I. Lee, L. Abraham, O. Alagoz, H. J. d. Koning, J. M. Hampton, L. Henderson, K. P. Lowry, *et al.*, "Breast cancer screening using mammography, digital breast tomosynthesis, and magnetic resonance imaging by breast density," *JAMA Internal Medicine*, Vol. 184, No. 10, 1222–1231, 2024.

[6] Boulerbah, R., A. Chaabane, I. Al-Naib, A. S. M. Alqadami, D. Aissaoui, and H. Attia, "Recent advancements in breast cancer detection: A holistic review of microwaves, ultrasound, and photo-acoustic imaging techniques," *IEEE Journal of Microwaves*, Vol. 5, No. 4, 776–792, 2025.

[7] De Jesus Aragão, A., D. Carvalho, B. Sanches, and W. A. M. V. Noije, "A review on microwave imaging systems for breast cancer detection," *IEEE Access*, Vol. 12, 190 611–190 628, 2024.

[8] Aboagye, S. O., J. A. Hunt, G. Ball, and Y. Wei, "Portable non-invasive technologies for early breast cancer detection: A systematic review," *Computers in Biology and Medicine*, Vol. 182, 109219, 2024.

[9] Han, B. B., S. K. Patel, A. Baldania, Y. Sharma, and F. A. Alzahrani, "Smart graphene-enhanced ceramic material refractive index sensor simulation design developed for highly sensitive breast cancer detection optimized with machine learning," *Spectrochimica Acta Part A: Molecular and Biomolecular Spectroscopy*, Vol. 356, 127742, 2026.

[10] Bhavani, M. V. L., D. Chaturvedi, T. Lanka, T. A. Raju, G. Rana, and A. Kumar, "A non-invasive microwave imaging system for breast tumor detection using a high gain vivaldi antenna array sensor," *IEEE Sensors Journal*, Vol. 25, No. 17, 32 631–32 640, 2025.

[11] Saeidi, T., S. N. Mahmood, S. Saleh, N. Timmons, A. J. A. Al-Gburi, and F. Razzaz, "Ultra-wideband (UWB) antennas for breast cancer detection with microwave imaging: A review," *Results in Engineering*, Vol. 25, 104167, 2025.

[12] Guetaf, B., A. Chaabane, A. Khalfallaoui, and H. Attia, "Narrow-band circularly polarized antenna for medical microwave imaging and health monitoring applications," *Applied Computational Electromagnetics Society Journal (ACES)*, Vol. 38, No. 6, 424–438, 2023.

[13] Mahfuz, M. M. H., A. M. Mahfouz, E. Baladi, and A. A. Kishk, "Microstrip patch antennas for breast tumor/cancer cell detection–challenges, designs, and future opportunities: A review]," *IEEE Access*, Vol. 12, 172 297–172 324, 2024.

[14] Chen, Q., X. Rao, D. Cao, Q. Huang, X. Xia, S. Wang, X. Zhang, Z. Cai, S. Chen, X. Peng, L. Meng, Z. Li, P. Zhang, and S. Han, "Real-time differentiation between benign and malignant breast tumors and other tissues using dielectric properties," *Medical Science Monitor: International Medical Journal of Experimental and Clinical Research*, Vol. 31, e947531, 2025.

[15] Fernández-Aranzamendi, E. G., P. R. Castillo-Araníbar, E. G. S. R. Castillo, B. S. Oller, L. Ventura-Zaa, G. Eguiluz-Rodriguez, V. González-Posadas, and D. Segovia-Vargas, "Dielectric characterization of ex-vivo breast tissues: Differentiation of tumor types through permittivity measurements," *Cancers*, Vol. 16, No. 4, 793, 2024.

[16] Hussein, M., F. Awwad, D. Jithin, H. E. Hasasna, K. Athamneh, and R. Iratni, "Breast cancer cells exhibits specific dielectric signature in vitro using the open-ended coaxial probe technique from 200 MHz to 13.6 GHz," *Scientific Reports*, Vol. 9, No. 1, 4681, 2019.

[17] Ali, U., A. Basir, M. Zada, S. Ullah, B. Kamal, and H. Yoo, "Performance improvement of a dual-band textile antenna for on-body through artificial magnetic conductor," *IEEE Access*, Vol. 11, 72 316–72 331, 2023.

[18] Boulerbah, R., A. Chaabane, H. Attia, and D. Aissaoui, "Breast cancer detection using circularly polarized printed UWB antenna," in *2023 2nd International Conference on Electronics, Energy and Measurement (IC2EM)*, 1–5, Medea, Algeria, 2023.

[19] Lanka, T., D. Chaturvedi, M. V. L. Bhavani, and A. Kumar, "Design of PRS enabled monopole slotted-antenna sensor for breast tumor detection," *Scientific Reports*, Vol. 15, No. 1, 19332, 2025.

[20] Subramanian, S., B. Sundarambal, and D. Nirmal, "Investigation on simulation-based specific absorption rate in ultra-wideband antenna for breast cancer detection," *IEEE Sensors Journal*, Vol. 18, No. 24, 10 002–10 009, 2018.

[21] Banu, M. A. S., S. Vanaja, and S. Poonguzhali, "UWB microwave detection of breast cancer using SAR," in *2013 International Conference on Energy Efficient Technologies for Sustainability*, 113–118, Nagercoil, India, 2013.

[22] Boulerbah, R., A. Chaabane, H. Attia, and D. Aissaoui, "Breast cancer detection using aperture coupled patch antenna," in *2024 3rd International Conference on Advanced Electrical Engineering (ICAEE)*, 1–4, Sidi-Bel-Abbes, Algeria, 2024.

[23] Aldhaeebi, M. A., T. S. Almoneef, H. Attia, and O. M. Ramahi, "Near-field microwave loop array sensor for breast tumor detection," *IEEE Sensors Journal*, Vol. 19, No. 24, 11 867–11 872, 2019.

[24] Mahfuz, M. M. H., M. R. Islam, M. H. Habaebi, N. A. Malek, and M. W. Sami, "Design of a flexible textile antenna for early breast tumor detections," in *2023 9th International Conference on Computer and Communication Engineering (ICCCE)*, 394–399, Kuala Lumpur, Malaysia, 2023.

[25] Elsaadi, M. and R. Hamad, "Breast cancer hyperthermia treatment based on slotted patch antenna at 2.45 GHz," *Circuits Syst*, Vol. 14, No. 5, 10–18, 2023.

[26] Bhavani, M. V. L., D. Chaturvedi, T. Lanka, and A. Kumar, "Development of a QMSIW antenna sensor for tumor detection utilizing a hemispherical multilayered dielectric breast-shaped phantom," *IEEE Sensors Journal*, Vol. 24, No. 20, 32 080–32 089, 2024.